RSC Advances

PAPER

View Article Online
View Journal | View Issue

Cite this: *RSC Adv.*, 2021, **11**, 24822

Construction of Z-scheme NiO/NiC/g-C_3N_4 composites using NiC as novel cocatalysts for the efficient photocatalytic degradation†

Xiaojie Song,‡ Sisi Ye,‡ Xin Zhou, Wanrui Gui, Can Yang and Zhihong Yang *

Received 7th May 2021
Accepted 24th June 2021

DOI: 10.1039/d1ra03562b

rsc.li/rsc-advances

A novel composite consisting of NiO/NiC/g-C_3N_4 with excellent photocatalytic properties was successfully synthesized by the simple calcination of layered double metal hydroxide (LDH) and melamine. The color and chemical composition of the as-prepared composites could be tailored by changing the mass ratio of NiAl-LDH and g-C_3N_4. For the L4C composite at the ratio of 1 : 1, it showed the desired dark color due to the generated NiC. It also showed high photodegradation efficiency under visible light irradiation, reaching 97.5% toward Rhodamine B and 92.6% toward tetracycline. The high photodegradation efficiency could be mainly attributed to the unique formation of NiC cocatalysts coupled with g-C_3N_4 and NiO semiconductors, which constructed a Z-scheme system and facilitated the efficient separation of the photogenerated electron–hole pairs. The present findings provide a promising approach for fabricating the new types of composite photocatalysts for pollutant degradation.

1. Introduction

With the development of human society, the problem of environmental pollution has aroused extensive attention and concern. Large amounts of synthetic dyes are consumed and discharged per year in various industries including textile, leather, paper, cosmetics and plastics.[1–3] Similarly, antibiotics, which are widely used to improve human and animal health and treat infections, are frequently discharged into surface water, seawater and groundwater.[4,5] The effluent organic wastewater without effective treatment severely pollutes water resources and ecosystems, and even threatens human health. So, the hazardous organic matter must be efficiently separated from the water before its discharge and many treatment technologies have been developed in recent years, such as physical methods (adsorption, membrane separation and magnetic separation), chemical methods (electrochemical process, photocatalytic oxidation, Fenton and Fenton-like oxidation and ozone oxidation), and biological methods (anaerobic method, aerobic method, anaerobic–aerobic combination process).[6] Among these wastewater treatment methods, photocatalytic degradation involving advanced oxidation processes is an energy-saving and highly effective technology using efficient photocatalysts under light irradiation.[7] The photocatalytic behavior is mainly determined by the quality of the photocatalyst; hence, various semiconductor-based materials have been explored for the photocatalytic degradation of organic pollutants.

Layered double metal hydroxides (LDH), which are hydrotalcite-like materials and a family of anionic clays, are among the most important photocatalysts intensively investigated for wastewater treatment.[8,9] LDH, often expressed by the general formula $[M_{1-x}^{2+}M_x^{3+}(OH)_2]^{x+}(A^{n-})_{x/n}\cdot mH_2O$, are characterized by positively charged metal hydroxide laminates and negatively charged balanced anions in the interlayer, with controllable composition and gallery spacing. LDH containing photo-active metal components (*e.g.*, Zn, Ni, Cr, or Fe) show photocatalytic properties and have been widely employed as heterogeneous catalysts, catalyst precursors or catalyst supports for environmental clean-up and energy production.[10,11] Moreover, when LDH is calcined at intermediate temperatures, the calcination products consist of poorly crystallized mixed metal oxides (MMOs) with many advantages in comparison to common metal oxides and LDH, such as the reconstruction of the layered structure by rehydration, a uniform distribution of metal cations at the atomic level and their adjustable components in a controllable manner.[12] However, LDH and LDH-derived MMOs are not highly efficient in photocatalytic processes due to the recombination of electron–hole pairs and the low utilization of visible light.[13]

Recently, 2D graphitic carbon nitride (g-C_3N_4) has attracted significant attention due to its simple synthesis, stable properties, suitable band energy, non-toxicity and high stability.[14,15] It also exhibits photocatalytic activities toward many organic pollutants[16,17] because of its appropriate band structure and

Faculty of Materials Science and Chemistry, Engineering Research Center of Nano-Geomaterials of Ministry of Education, China University of Geosciences, Wuhan, 430074, China. E-mail: yzhh05@126.com; Tel: +86-27-67884814

† Electronic supplementary information (ESI) available. See DOI: 10.1039/d1ra03562b

‡ Both authors contributed equally to this work.

strong light absorption ability. However, its catalytic efficiency is quite low due to the inadequate utilization of visible light and the rapid recombination of photogenerated electrons and holes.[18,19] It has been identified that its catalytic efficiency can be improved by coupling with other semiconductor photocatalysts *via* transferring the photogenerated electron–hole pairs between g-C_3N_4 and other semiconductors to depress the charge recombination.[17]

Recently, it was confirmed that the lifetimes of photogenerated charge carriers increased and visible-light-induced photocatalytic properties were enhanced when g-C_3N_4 was incorporated with LDH or LDH-derived MMOs. *E.g.*, through the formation of 2D/2D interface heterostructures, g-C_3N_4/NiAl-LDH,[20–22] g-C_3N_4/ZnTiLDH,[23] g-C_3N_4/ZnAl-LDH,[15] g-C_3N_4/NiFe-LDH[19] and g-C_3N_4/CoFe-LDH[13] composites were synthesized with improved visible-light-driven performance, much better than that of either single-phase g-C_3N_4 or LDH. Moreover, when the precursor of g-C_3N_4 was mixed with LDH and then calcined, MMOs/g-C_3N_4 composites were obtained and the photocatalytic efficiency was promoted. *E.g.*, Di[24] reported that the coupling of ZnFe-MMOs (ZnO and $ZnFe_2O_4$) with g-C_3N_4 was beneficial to the degradation of ibuprofen (IBF) and sulfadiazine (SDZ). Lan[12] identified that the obtained nanocomposites of ZnIn-MMOs (In_2O_3 and ZnO) and g-C_3N_4 exhibited improved photodegradation activity toward Rhodamine B (RhB) under visible light irradiation. Patnaik[25] found that the incorporation of ZnCr-MMOs ($ZnCr_2O_4$ and ZnO) and g-C_3N_4 exhibited good H_2 and O_2 production. From these reports, it can be seen that MMOs and g-C_3N_4 products were detected from the calcination of g-C_3N_4 precursor and LDH with the enhancement of photocatalytic properties. However, whether metal carbides as the possible derived products would present and how these metal compounds affect the photocatalytic efficiency were unclear.

Some transition-metal carbides with the benefits of relative earth abundance, such as Ni_3C,[27,28] WC,[29] Mo_2C[30] and Ti_2C_3 (ref. 31) have been identified to be potential photocatalysts or electrocatalysts.[26] Nickel carbides (NiC_x) with superior electric conductivity provide the possibility to fabricate the catalysts or cocatalysts with high performance and cost-effectiveness.[32] A series of nickel carbides including $NiC_{0.2}$,[33] NiC,[34,35] and Ni_3C[36–38] with different crystal structures were synthesized for water-splitting catalysts and showed good catalytic activity. However, to the best of our knowledge, most of these reports were focused on their electrocatalytic performances for hydrogen evolution applications, and very limited reports addressed their applications as promising photocatalysts. Therefore, exploring the photocatalytic activity of nickel carbides is of great importance to seeking valuable alternative cocatalysts for high photocatalytic efficiency.

In this paper, NiC, NiO, and g-C_3N_4 products were successfully synthesized by the simple calcination of a NiAl-LDH and melamine mixture. This obtained novel composite combines the unique properties of nanostructured conductors (NiC) and semiconductors (NiO and g-C_3N_4), showing significantly improved photocatalytic activity in degrading organic Rhodamine B (RhB) dye and tetracycline (TC) in comparison to pure NiAl-MMO and g-C_3N_4. This work provides a controllable and mild strategy for the design and preparation of fascinating NiC-containing photocatalysts that can serve as promising candidates in photodegradation and photocatalytic H_2 evolution.

2. Experimental

2.1 Preparation of photocatalysts

2.1.1 Materials. All materials used in this research were of analytical grade and used as received. All chemicals were purchased from Sinopharm Chemical Reagent Co. Ltd., including aluminum nitrate ($Al(NO)_3 \cdot 9H_2O$), nickel nitrate ($Ni(NO_3)_2 \cdot 6H_2O$), urea (CH_4N_2O), and melamine ($C_3N_3(NH_2)_3$).

2.1.2 Synthesis of NiAl-LDH. NiAl-LDH was synthesized by a hydrothermal method.[39] Here, 0.75 g of $Al(NO)_3 \cdot 9H_2O$ and 1.75 g of $Ni(NO_3)_2 \cdot 6H_2O$ were added to 40 mL of deionized water with stirring for 30 min until they dissolved completely. Subsequently, 2.4 g of urea was added to the mixture with stirring for 30 min. Then the mixture was transferred into a 100 mL Teflon-lined autoclave and heated at 120 °C for 12 h. After cooling to room temperature, the white solid was collected by high-speed centrifugation and washed with deionized water until the pH reached 7. Finally, the collected solid was dried at 60 °C for 10 h in a vacuum drying oven to obtain NiAl-LDH.

2.1.3 Synthesis of NiO/NiC/g-C_3N_4 composites. The NiO/NiC/g-C_3N_4 composites were synthesized by calcination treatment. Melamine was mixed with the as-prepared NiAl-LDH in ball milling for 2 h and then put in the crucible covered with aluminum foil. Subsequently, the crucible was calcined at 550 °C for 4 h at a heating rate of 2 °C min^{-1} in the muffle furnace to obtain the products. According to the mass proportions of NiAl-LDH and melamine at 1 : 6, 1 : 5, 1 : 3, 1 : 1, 1 : 0.5, the corresponding products were labeled as L1C, L2C, L3C, L4C, L5C, respectively. L was for the NiAl-LDH, the C was for the g-C_3N_4. For comparison, the sample produced from pure NiAl-LDH was labeled as NiAl-MMO.

2.2 Characterization

X-ray powder diffraction (XRD) patterns were examined on a Bruker D8-ADVANCE powder X-ray Diffractometer at 200 mA and 40 kV using Cu Kα radiation ($\lambda = 0.15406$ nm) over the 2θ range of 5–90°, and FT-IR spectra were recorded by using a Perkin-Elmer 100 spectrometer in the range of 4000–500 cm^{-1} using the KBr disc technique. The morphologies of the samples were determined by scanning electron microscopy (Hitachi SU-70 SEM). The ultraviolet-visible diffuse reflectance spectra (UV-vis DRS) of samples were recorded over the range of 200–800 nm using a UV-2600. X-ray photoelectron spectroscopy (XPS) was characterized with EscaLab Xi^+ equipment with Al Ka radiation ($h\nu = 1486.6$ eV). The distribution characterization was further analyzed by a transmission electron microscope (TEM, Talos F200X) equipped with energy dispersive X-ray (EDX). The Brunauer–Emmett–Teller (BET) analysis was carried out *via* N_2 adsorption using (SSA-7000), in which the Barrett–Joyner–Halenda (BJH) method was followed to analyze the pore size distribution. Photoluminescence (PL) spectra of the samples were obtained at room temperature on a steady-state

spectrofluorometer (SHIMADZU RF-6000) with an excitation wavelength of 330 nm. The electrochemical impedance spectroscopy (EIS) measurements were performed in the presence of a 0.1 M Na_2SO_4 solution with the frequency range of 0.1–100 kHz under open-circuit potential conditions (CHI 760E). Pt and Ag/AgCl electrodes were used as the counter electrode and reference electrode, respectively; the working electrode was prepared by loading a catalyst on ITO glass. Here, 10 mg of the catalyst was dispersed in 300 μL ethanol and 100 μL Nafion ionomer solution (2 wt%), then ultrasonicated for 30 min to form a uniform suspension. Next, 100 μL of the suspension was dropped on the ITO glass to form a 0.5 cm × 0.5 cm square and dried at room temperature. The electron spin resonance (ESR) spectra were determined using a Bruker EMXPLUS spectrometer.

2.3 Photocatalytic tests

The photocatalytic degradations of organic dyes and an antibiotic were performed under visible light irradiation. In the experiment, 50 mg of catalyst was dispersed in 40 mL aqueous solutions containing the dye or tetracycline at different concentrations. Prior to irradiation, the mixture dispersion was magnetically stirred for 15 min in the dark to establish the adsorption–desorption equilibrium. Under the irradiation from a 300 W Xe arc lamp, 3 mL of the reaction solution was withdrawn at 30 min intervals and filtered with a 0.45 μm microporous membrane to remove the photocatalyst, then the absorbances of RhB, TC, and methyl orange (MO) were measured by UV-Vis spectroscopy at wavelengths of 554, 357 and 460 nm, respectively.

3 Results and discussion

3.1 Structural characterization of NiO/NiC/g-C_3N_4 composites

Fig. 1 shows XRD patterns of all the samples. As shown in Fig. 1a, the pure g-C_3N_4 exhibited (100) and (002) diffraction peaks at 13.1° and 27.6°, corresponding to the characteristic interlayer stacking of the conjugated aromatic systems and in-planar structure repeating unit, respectively.[40–42] For pure NiAl-LDH, the characteristic diffraction peaks at 2θ angles below 30° correspond to the (003) and (006) planes,[43,44] indicating the regular two-dimensional hydrotalcite-like layered structure. When NiAl-LDH was calcinated into NiAl-MMO, the characteristic diffraction peaks of (003) and (006) reflecting the interlayer structure disappeared, while the diffraction peaks at 37.04°, 44.32° and 62.69° appeared, which are ascribed to the (111), (200) and (220) of NiO planes,[45] respectively.

When NiAl-LDH and melamine are mixed at suitable mass ratios, it is interesting that in addition to g-C_3N_4, the generated products consist of NiO and NiC, and a small amount of Ni_3N; the corresponding crystal plane peaks of NiC are the (111) and (200), and the peak of Ni_3N is (111), different from the only metal oxide phase in other reports.[46] Al-containing compounds were not detected in all samples, which may be attributed to their low content or amorphous structure. As the amount of melamine decreased, the peak of g-C_3N_4 (002) gradually decreased; for the L1C samples with high melamine content and L4C, L5C with high NiAl-LDH, the main phases are g-C_3N_4 and NiAl-MMO, respectively.

Fig. 2 presents the FT-IR patterns of the synthesized g-C_3N_4, NiAl-MMO, and NiO/NiC/g-C_3N_4 composites. For the pure g-C_3N_4, the band at 811 cm^{-1} is attributed to the breathing vibration of the triazine heterocycle,[47,48] and the broad absorption band at 3300 cm^{-1} corresponds to the stretching vibration of N–H. In addition, the bands between 1200 and 1700 cm^{-1} are assigned to the typical C–N and C=N stretching modes of the triazine ring.[49] For the NiAl-MMO sample, the bands at 3450 and 1636 cm^{-1} can be assigned to the O–H stretching and bending vibrations, respectively. The band at 1415 cm^{-1} may correspond to the bending vibrations of NO_3^- ions intercalated in the layer of NiAl-LDH.[50] The other bands below 800 cm^{-1} are

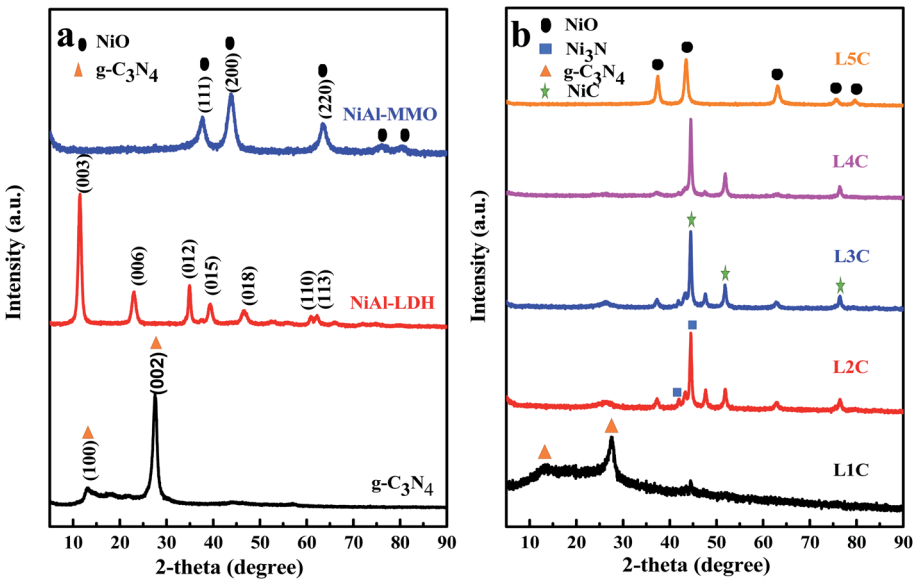

Fig. 1 XRD patterns of the synthesized samples, (a) g-C_3N_4, NiAl-LDH, NiAl-MMO, and (b) NiO/NiC/g-C_3N_4 composites.

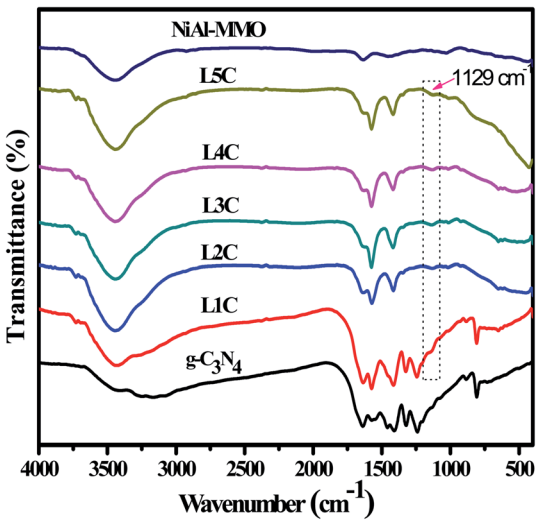

Fig. 2 FT-IR patterns of g-C_3N_4, NiAl-MMO and NiO/NiC/g-C_3N_4 composites.

attributed to the translational modes of metal–oxygen (Ni–O and Al–O) and metal–oxygen–metal (Ni–O–Al) bands.[51] Compared with NiAl-MMO and g-C_3N_4, the NiO/NiC/g-C_3N_4 composites showed a new weak peak at 1129 cm^{-1}, which may be related to the formation of NiC.

Fig. 3 shows SEM images of g-C_3N_4, NiAl-LDH, NiAl-MMO, and NiO/NiC/g-C_3N_4 samples. It can be seen that the bulk g-C_3N_4 sample exhibited serious aggregation. The NiAl-LDH sample displayed a 3D flaky morphology with plenty of thin nanoflakes, and the NiAl-MMO sample showed a similar flower-like morphology with decreased particle size. For the L1C sample, a large number of plate-like particles were observed, which consist of g-C_3N_4 lamellas based on the above XRD analysis. For the L5C sample, more 2D flakes were observed and they showed the tendency to develop into flower-like shapes, similar to the morphology of pure NiAl-MMO. For L2C, L3C, and L4C samples, in addition to flake-like particles, more granular particles were detected with the sharply decreased size. Particularly, the morphology of L4C samples at high magnification showed that the lamellas were mixed with many small nanoparticles, suggesting that g-C_3N_4 and NiO semiconductors with two-dimensional lamella structure were well coupled with zero-dimensional NiC conductors with the formation of the heterojunction.

In Fig. 4, the TEM image of the L4C sample reveals that the nanoparticles with diameters of 5–50 nm were distributed on

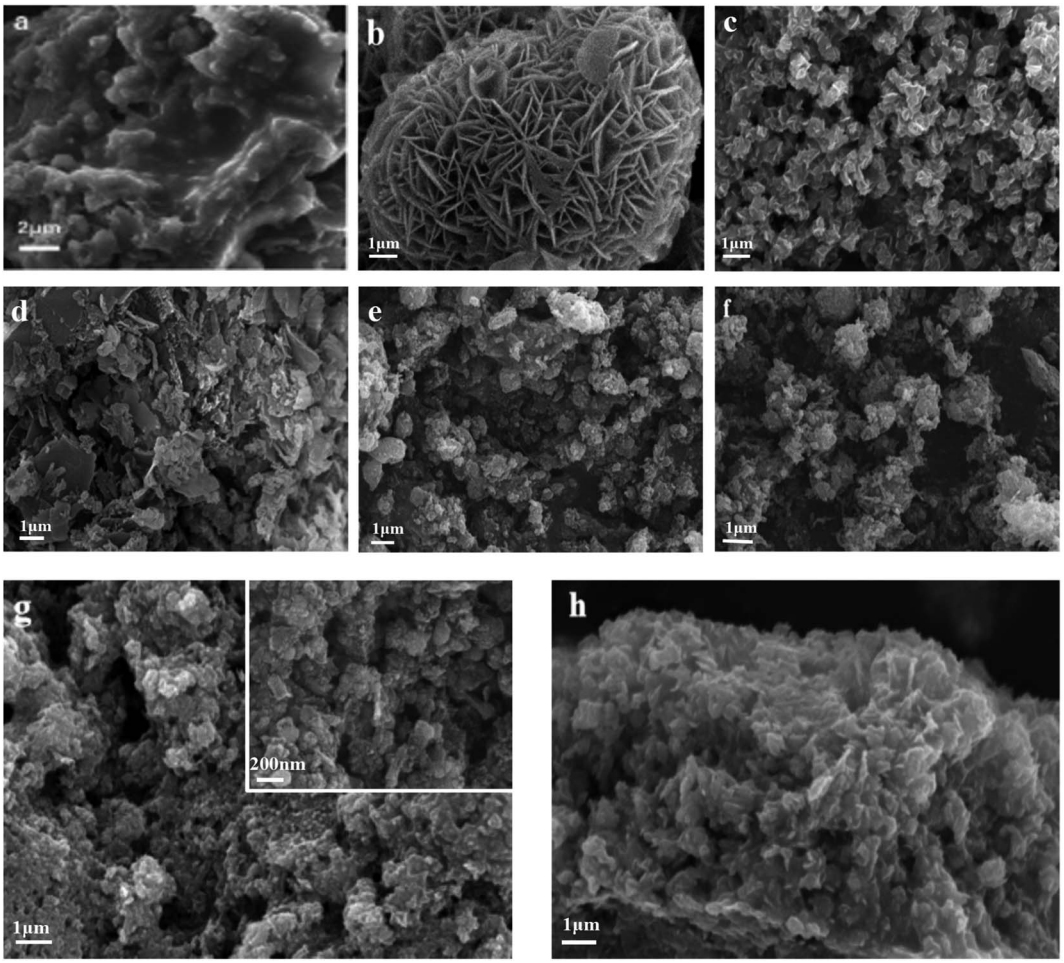

Fig. 3 SEM image of the samples, (a) g-C_3N_4, (b) NiAl-LDH, (c) NiAl-MMO, (d) L1C, (e) L2C, (f) L3C, (g) L4C, (h) L5C.

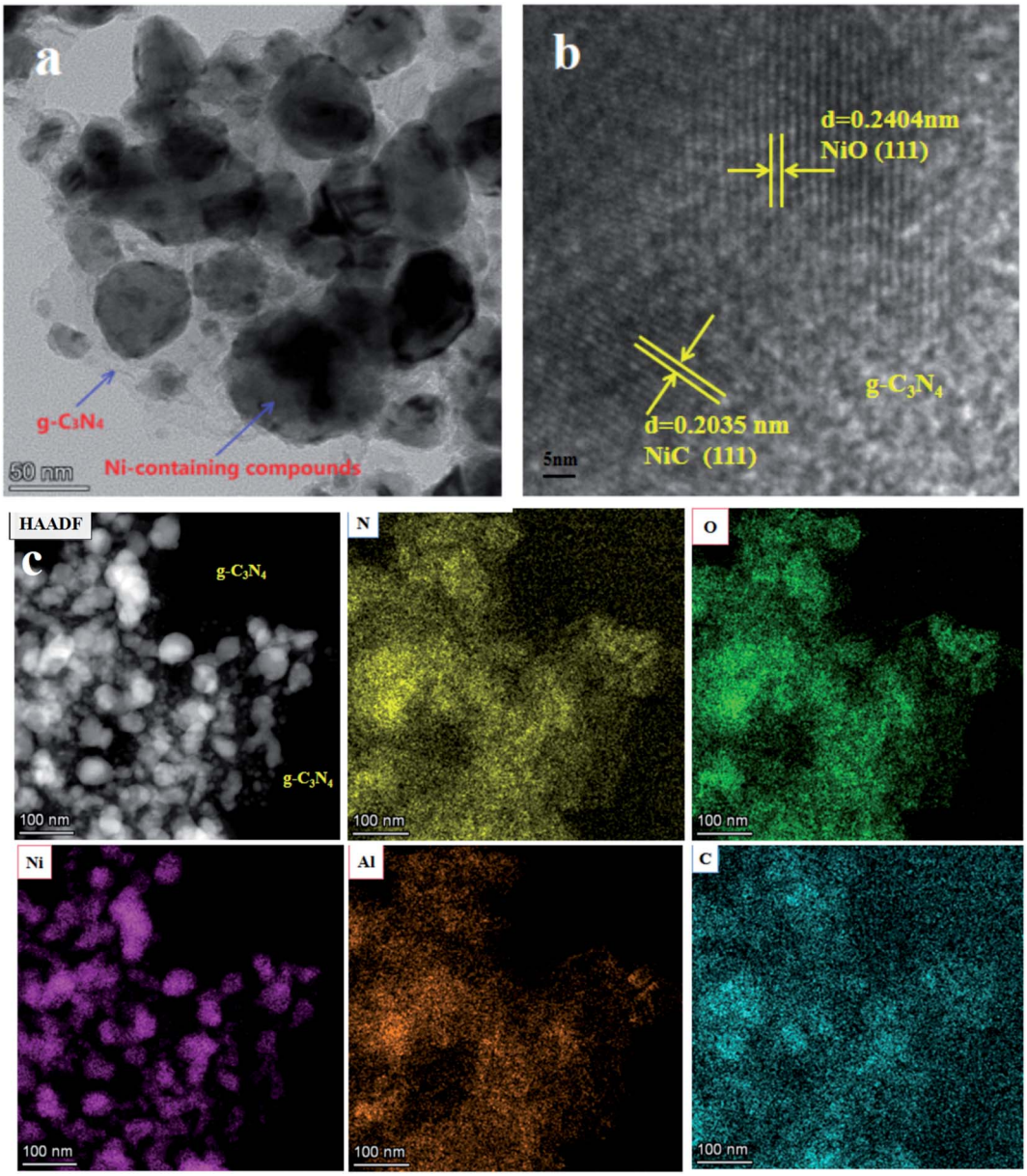

Fig. 4 Characterization of the L4C sample: (a) TEM image, (b) high-resolution TEM image, (c) HAADF-STEM images and the corresponding element maps of N, O, Ni, Al, and C.

a cotton-like g-C_3N_4 matrix.[24] HRTEM images presented the lattice fringes of these nanocrystals. The *d*-spacings of 0.2404 and 0.2035 nm were indexed as the (111) facets in NiO and NiC crystals, respectively, and the fluffy part is attributed to g-C_3N_4. These different types of nanocrystals formed intertwined structures, identifying the formation of closely linked heterojunctions. The corresponding element maps show that the bright nanoparticles in the HAADF image were mainly composed of nickel-containing compounds with a small number of aluminum compounds. Moreover, C and N element maps indicated that the dark regions in the HAADF image were covered with g-C_3N_4 nanosheets, further indicating that nickel-containing nanoparticles were homogeneously distributed on the surface of g-C_3N_4 sheets.[52]

The XPS spectra were obtained to analyze the detailed chemical status of the composite photocatalysts. In Fig. 5, the XPS spectrum of the L4C sample exhibits peaks corresponding to Ni, Al, C, N, and O elements. The Ni 2p spectrum displays two peaks with the binding energies of 853.9 and 872.7 eV, corresponding to Ni $2p_{3/2}$ and Ni $2p_{1/2}$, respectively, which reflects the typical binding energies of Ni^{2+} in the L4C composite. Moreover, Ni $2p_{3/2}$ can be deconvoluted into three peaks at the binding energies of 854.2 and 856.6 eV, corresponding to Ni^{2+} in NiO, and Ni^{3+} in NiC compounds,[53,54] respectively, in agreement with the XRD pattern results as discussed above. The appearance of Ni^{3+} is probably due to the existence of nickel vacancies and oxygen vacancies along with the oxidation of surface Ni^{2+} to Ni^{3+} to achieve charge neutrality during the calcination

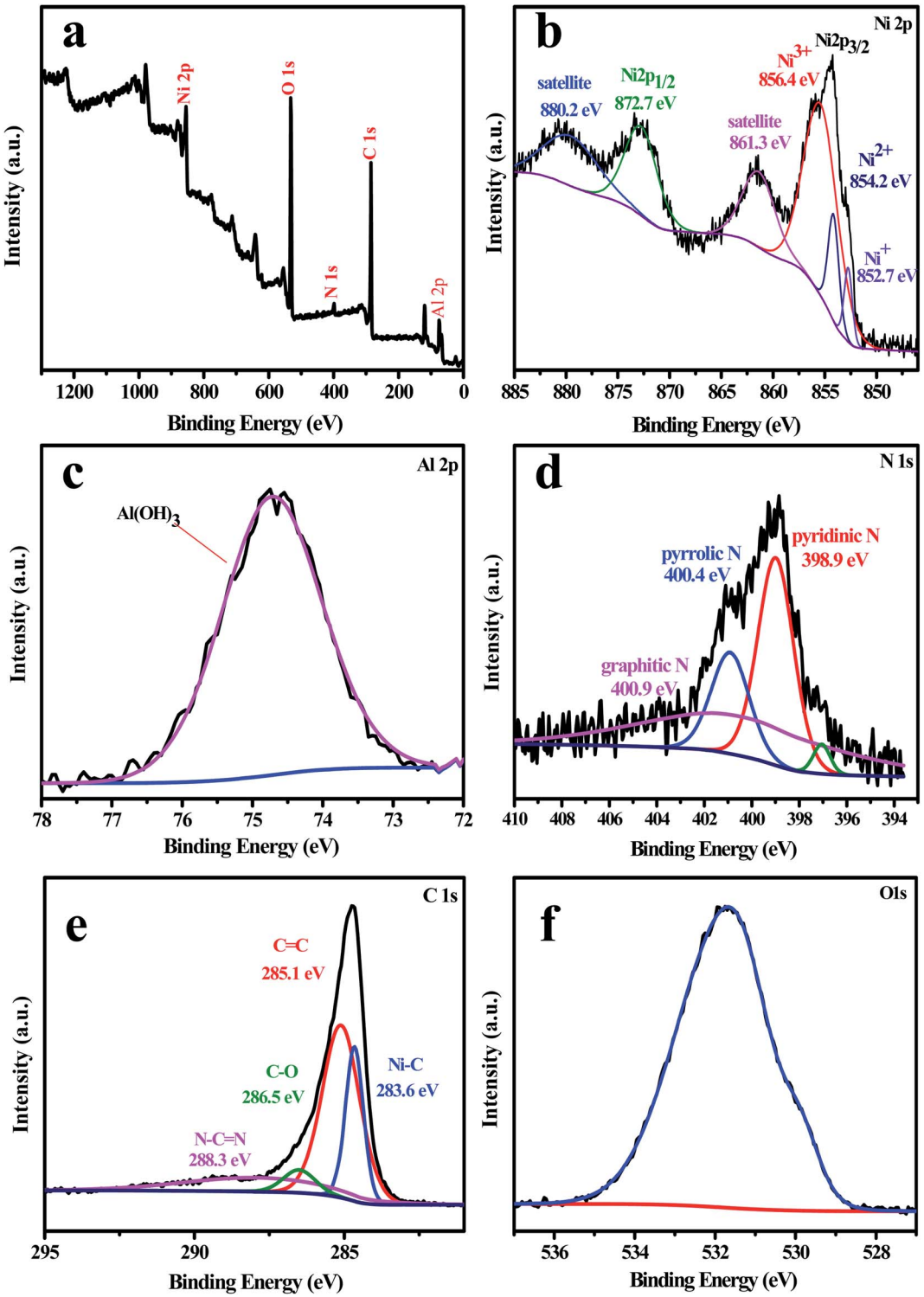

Fig. 5 XPS profile spectra of the L4C sample: (a) survey spectrum, (b) Ni 2p, (c) Al 2p, (d) N 1s, (e) C 1s, (f) O 1s.

process.[55] The N 1s spectrum can be fit to four peaks. The one located at 397.1 eV may be associated with N–Ni,[53,56] and the other three at 398.9, 400.4, and 400.9 eV were assigned to sp^2-hybridized nitrogen in triazine rings (C–N=C), bridged tertiary nitrogen N–$(C)_3$ groups, and amino functional groups (N–H), respectively.[20] The C 1s spectrum showed four deconvoluted peaks located at 283.6, 285.1, 286.5, and 288.3 eV (Fig. 5e).[20,57,58] The peaks at 283.6 and 285.1 eV were assigned to NiC and sp^2-hybridized carbon atoms in C–C bonds, respectively.[59] The peaks at 286.5 and 288.3 eV were assigned to the C–O functional group[59] and the sp^2-hybridized carbon bonded to N inside the triazine rings,[57,60] respectively. The XPS spectrum of O 1s located

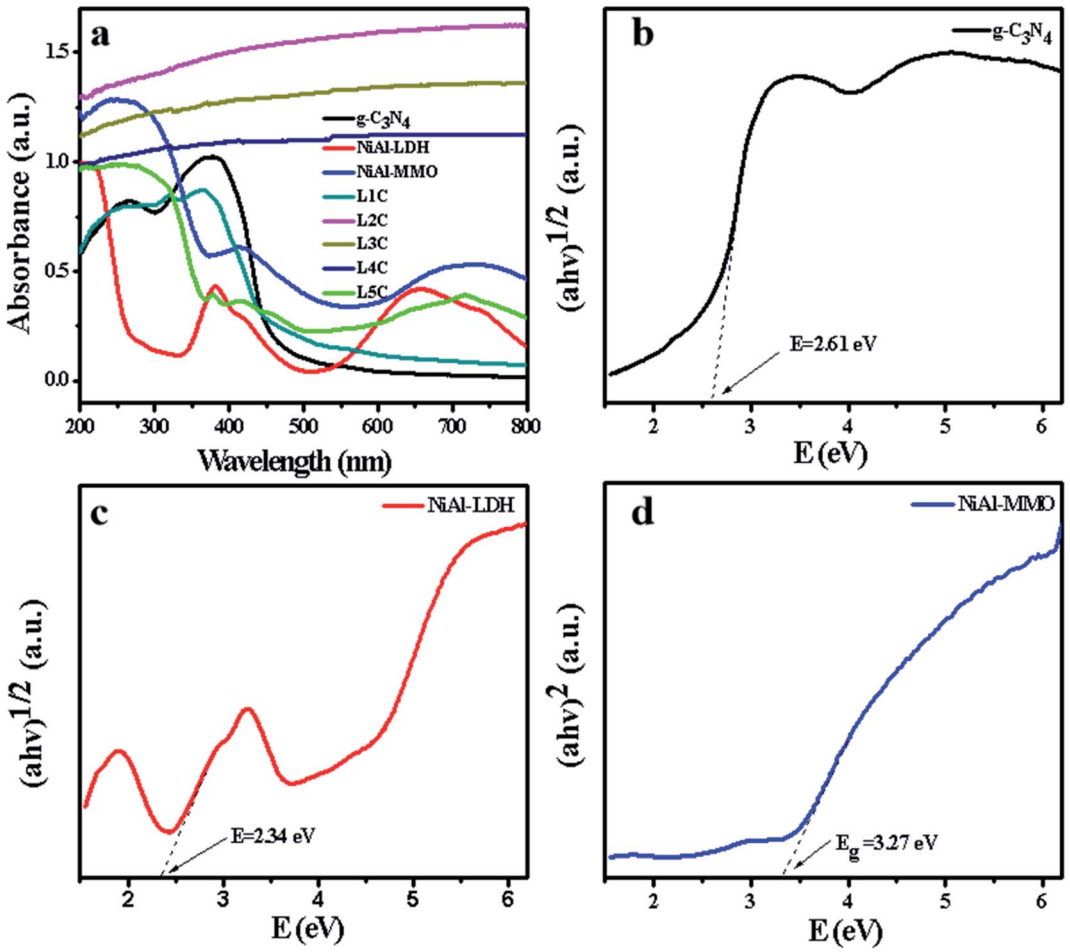

Fig. 6 UV-Vis DRS of the synthesized samples (a), and the band gaps of the synthesized g-C_3N_4 (b), NiAl-LDH (c), and NiAl-MMO (d).

at 531.65 eV is related to hydroxide ions[61] and the Al 2p spectrum may be ascribed to Al_2O_3 produced from the calcination of NiAl-LDH.[62]

Fig. S1† shows the colors of all the samples. Compared with yellow g-C_3N_4 and green NiAl-MMO, the NiO/NiC/g-C_3N_4 composites became much darker. Particularly, the samples including L2C, L3C, and L4C are exclusively black due to the presence of black NiC and NiO nanoparticles,[63] which would significantly promote the absorption of visible light.

The photoabsorption properties of g-C_3N_4, NiAl-LDH, and NiO/NiC/g-C_3N_4 were examined by UV-VIS DRS (Fig. 6). The pure g-C_3N_4 exhibited a typical semiconductor-like absorption in the

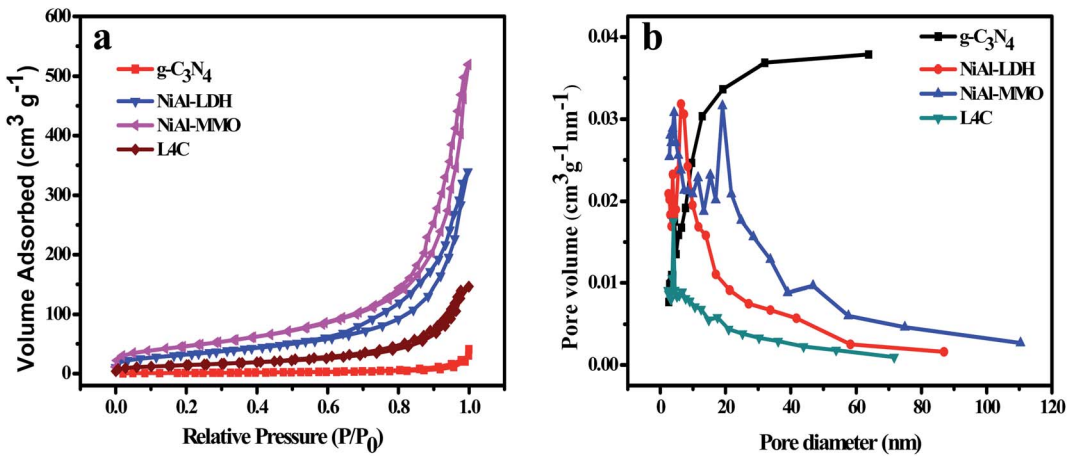

Fig. 7 (a) N_2 adsorption–desorption isotherms and (b) pore size distribution curves of g-C_3N_4, NiAl-LDH, NiAl-MMO, and L4C.

Table 1 BET surface areas and pore parameters of samples

Samples	S_{BET} (m^2 g^{-1})	V_{total} (cm^3 g^{-1})	$D_{average}$ (nm)
g-C_3N_4	5.09	0.06	25.03
NiAl-LDH	118.21	0.52	8.88
NiAl-MMO	167.86	0.80	9.56
L4C	82.55	0.23	8.59

blue region of the visible spectrum, and the absorption edge was around 460 nm, which may be assigned to n-π* transitions of the lone pairs on the edge of the N-atom of the triazine rings. The bandgap of g-C_3N_4 was calculated by using the equation $E_g = hc/\lambda$ and was found to be approximately 2.61 eV. In addition, the pure NiAl-LDH mainly showed three characteristic absorption bands in the UV and visible regions, where the first one is located from 200 to 300 nm, the second one from 300 to 500 nm, and the third one from 600 to 800 nm. For the synthesized NiAl-MMO, three similar absorption bands were detected with obvious optimal red-shifts and enhanced absorption intensity. It can be concluded that the bandgap of NiAl-MMO was about 3.27 eV, close to the bandgap of pure NiO in the literature,[64,65] further indicating that NiAl-MMO was mainly composed of NiO.

Among the as-prepared NiO/NiC/g-C_3N_4 samples, L1C and L5C nanocomposites showed absorption features similar to g-C_3N_4 and NiAl-MMO, respectively. However, the absorption spectra of L2C, L3C, and L4C are significantly different from other samples, showing approximate straight lines with no obvious absorption edges in the region ranging from 200 to 800 nm, which is attributed to their dark color as well as the typical metallic character of NiC.[66] Therefore, the formation of NiC nanoparticles could effectively increase the absorbance of visible light, and thus favors the photocatalytic properties of the nanocomposites.

The BET surface area distribution, pore volume and average pore size of g-C_3N_4, NiAl-LDH, NiAl-MMO and L4C materials were studied by N_2 adsorption/desorption isotherms (Fig. 7), and the results are summarized in Table 1. All the physical adsorption isotherms showed typical type IV adsorption behavior with H_3 hysteresis loops. The BET surface areas of g-C_3N_4, NiAl-LDH, NiAl-MMO and L4C were 5.09, 118.21, 167.86 and 82.55 m^2 g^{-1}, respectively; the total pore volume of the g-C_3N_4 (0.06 cm^3 g^{-1}) was lower than that of other samples. The surface area and pore volume of NiAl-MMO were well above that of NiAl-LDH, which could be due to the elimination of interlayer water during the calcining process. In addition, the surface area of L4C (82.55 m^2 g^{-1}) decreased as comparison with NiAl-MMO (167.86 m^2 g^{-1}), this is due to g-C_3N_4 having a higher proportion, resulting in a smaller specific surface area.

EIS (electrochemical impedance spectroscopy) Nyquist spectra at open-circuit voltage were employed to investigate the charge transfer and recombination behavior of the nanocomposites.[67] The semicircle of the high-frequency region on the EIS plots is related to the charge transfer resistance in the electrode reaction. The smaller the semicircle, the faster the charge transfer rate. In Fig. 8a, compared with other samples, L4C showed a small semicircle diameter, indicating its low interfacial charge transfer resistance. This is attributed to the presence of metallic NiC that rapidly transfers the photo-generated electrons and hence accelerates the separation of electrons and holes.

The separation of the photo-generated carriers for the hybrids can be further analyzed by photoluminescence (PL). Fig. 8b shows the photoluminescence spectra of the samples. Compared with other samples, the g-C_3N_4 sample showed a strong emission peak at 330 nm due to its terrible recombination of photogenerated electrons and holes. The inset graph shows that the emission peak of L4C is weaker than those of NiAl-LDH and NiAl-MMO, suggesting that the recombination of photogenerated carriers can be effectively restrained through the desired hybridization between g-C_3N_4, NiO, and NiC.

3.2 Photocatalytic activity of NiO/NiC/g-C_3N_4 composites

The photodegradation behavior of the as-prepared NiO/NiC/g-C_3N_4 photocatalysts was evaluated by Rhodamine B dye in the solution of concentration 10 mg L^{-1} under visible light irradiation. For comparison, the photocatalytic properties of pure g-C_3N_4 and NiAl-LDH were also tested. As shown in Fig. 9a and b, the degradation efficiencies of g-C_3N_4, NiAl-LDH and NiAl-MMO were 58%, 34.6% and 41.5% within 90 min, respectively. Compared with these photocatalysts, the photocatalytic ratios of the NiO/NiC/g-C_3N_4 composites were significantly improved, reaching 77.7%, 87.4% and 95.5% for L1C, L2C and L3C, respectively. Particularly, the L4C sample showed complete degradation activity with a degradation ratio close to 100%. However, the photocatalytic activities of L5C greatly decreased, which was attributed to the very low contents of NiC and g-C_3N_4 in the composites. Moreover, the reaction rate constant was determined using the first-order reaction kinetics equation by fitting the kinetic data *via* a linear plot of $\ln(C_0/C_t)$ against time. As shown in Fig. 9c, the RhB photocatalytic degradation behaviors well match the pseudo-first-order reaction dynamic model. Concretely, the photodegradation rate constant over L4C was 0.06795 min^{-1}, which is 7.3 and 12.7 times higher as compared to g-C_3N_4 and NiAl-MMO, respectively.

Since RhB at a concentration of 10 mg mL^{-1} was almost completely degraded by the L4C sample, the solutions with higher concentrations were prepared to further explore the degradation performance. In Fig. 9d, for the solution at concentrations of 30, 50, and 90 mg mL^{-1}, the degradation efficiencies of L4C were 97.5%, 76.6% and 46.6% within 120 min, respectively. Therefore, the degradation ratio decreased with the increase of the dye concentration and RhB can be completely degraded in the solution with a concentration of less than 30 mg mL^{-1}. Compared with g-C_3N_4 and Ni-containing photocatalysts toward RhB in the literature (Table 2), the L4C composite showed good photodegradation performance in this study.

The photocatalyst may be deactivated due to the combination of secondary products or oxidized intermediates. Cycling tests were operated to evaluate the stability and reusability of the L4C sample under visible light irradiation. After 90 min of

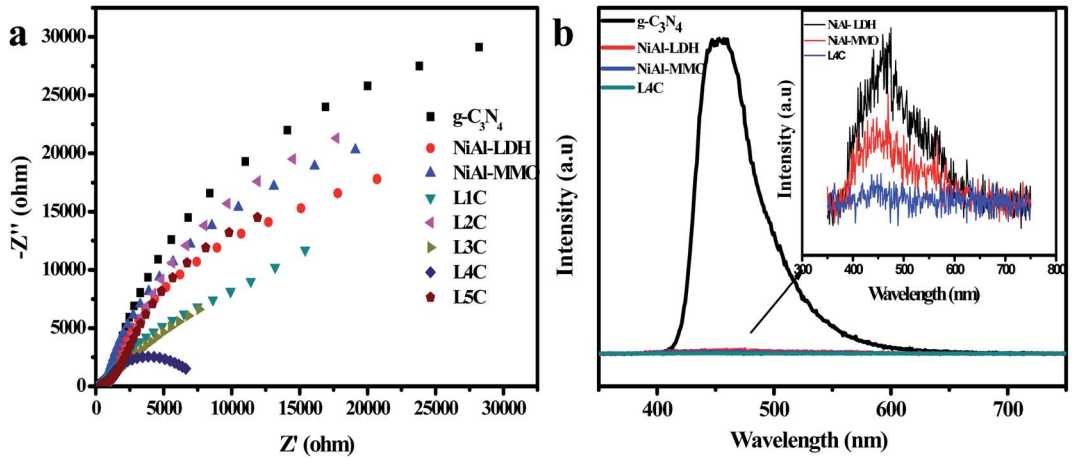

Fig. 8 (a) EIS Nyquist plots of all the samples. (b) PL spectra of the g-C_3N_4, NiAl-LDH, NiAl-MMO, and L4C samples.

irradiation in each cycle, the photocatalyst was separated from the aqueous suspension by centrifugation and washing with deionized water. Fig. 10a shows that this photocatalyst was successfully cycled for 6 successive cycles with a small loss of its initial catalytic activity, indicating that the obtained photocatalyst has both good stability and a long lifetime. As shown in Fig. 10b, the XRD spectrum of the L4C sample after six cycles was almost the same as that of the sample before cycling tests,

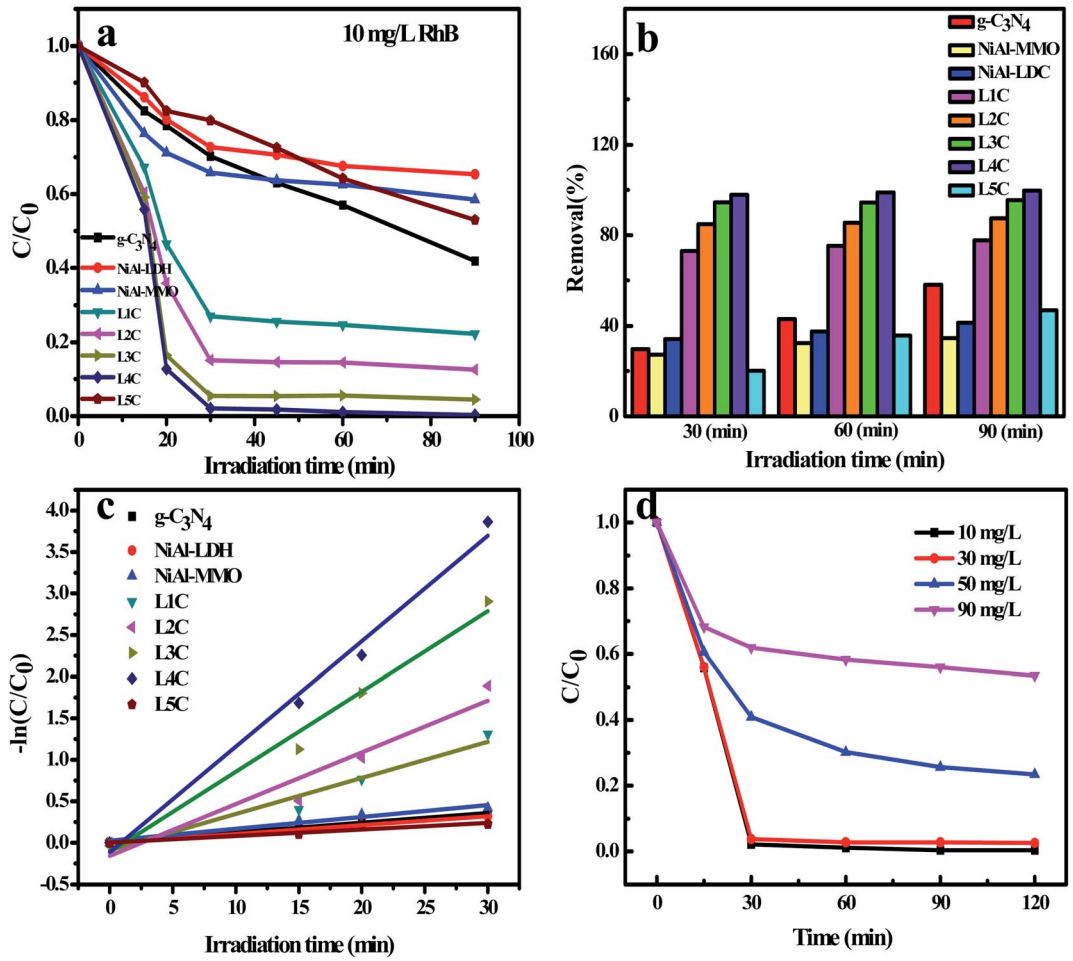

Fig. 9 (a and b) The photocatalytic degradation of 10 mg L^{-1} RhB dye by using different samples (dosage: 50 mg); (c) the pseudo-first-order kinetic fitting curve; (d) the degradation of RhB with different concentrations by using L4C.

Table 2 Comparison of the degradation efficiencies of representative photocatalysts

Photocatalyst	Dye	Light source	Dye (mg L^{-1}) of solution	Time (min)	Rate of (%) degradation	References
g-C_3N_4	RhB	Visible	10	120	90.08	57
g-C_3N_4-40@NiAl-LDH	RhB	Visible	20	240	99	53
NiO@g-C_3N_4	RhB	Visible	30	20	75.2	54
Ni/NiO/TiO_2	RhB	Visible	2	30	99	55
Ag/NiAl-LDH/g-C_3N_4	RhB	Visible	5	60	99	56
NiAl-MMO/g-C_3N_4	RhB	Visible	10	90	99	This paper

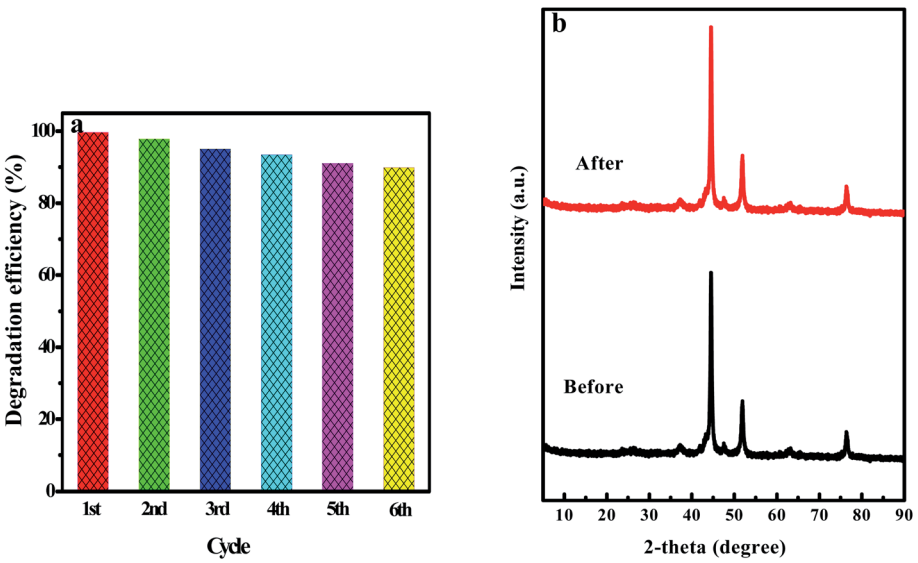

Fig. 10 (a) Recycled runs for the photocatalytic degradation of 10 mg L^{-1} RhB by using the L4C composite. (b) XRD patterns of L4C before and after recycling.

further indicating that the composite has good photostability and chemical stability under the studied conditions.

3.3 Photocatalytic activity of the composites toward MO and TC

To investigate the photodegradation behaviors of L4C toward other organic pollutants, TC antibiotic and the anionic MO dye were employed at the concentrations of 30 mg L^{-1} and 10 mg L^{-1}, respectively. In Fig. 11a, the photodegradation ratio of MO is low (13%) for L4C and almost no photodegradation was detected for g-C_3N_4 and NiAl-MMO. Additionally, a higher absorption ratio of NiAl-LDH was detected in the adsorption stage and then a small decrease was observed under the irradiation of visible light, indicating the significant absorption ability of NiAl-LDH with poor photocatalytic ability. For comparison, the adsorption experiment without light irradiation was carried out simultaneously and the results showed that the adsorption ratio was almost the same as that from the photodegradation experiment (Fig. 11b), further identifying the good absorption and poor photodegradation ability of NiAl-LDH. These results can be explained by the fact that the absorbance and photodegradation performance of these samples are severally affected by the surface charge properties, which were evaluated *via* the zeta potentials. In Fig. 11c, L4C, NiAl-MMO, and g-C_3N_4 are negatively charged, but NiAl-LDH is positively charged (3.61 mV) due to the positive charge of its brucite-like layer.[68,69] Cationic MO is easily adsorbed on the surface of NiAl-LDH nanoparticles through electrostatic attraction and is rejected by L4C and g-C_3N_4 samples through electrostatic repulsion, so it is not efficient to employ these samples as the photocatalyst to degrade anionic organic pollutants.

Fig. 11d and e show the photocatalytic ratios and reaction rate constants toward antibiotic TC, respectively. In the solution with a TC concentration of 30 mg L^{-1}, L4C exhibited a high photocatalytic ratio (92.6%) and reaction rate constant (0.0209) in comparison with NiAl-LDH and g-C_3N_4, reflecting the good photodegradation due to the synergetic enhancement of NiO, NiC, and C_3N_4. Interestingly, NiAl-MMO also showed good adsorption but poor photodegradation toward TC, which was identified by the adsorption experiment in Fig. 11f. The good adsorption of NiAl-MMO may be attributed to the abundant surface hydroxyl groups of the mixed oxides, which form hydrogen bonds with the hydroxyl of the TC molecule.

3.4 The photocatalytic mechanism of NiO/NiC/g-C_3N_4 composites

As shown in Fig. 12, the heterogeneous catalysts including g-C_3N_4, NiO and NiC simultaneously appeared in the as-prepared

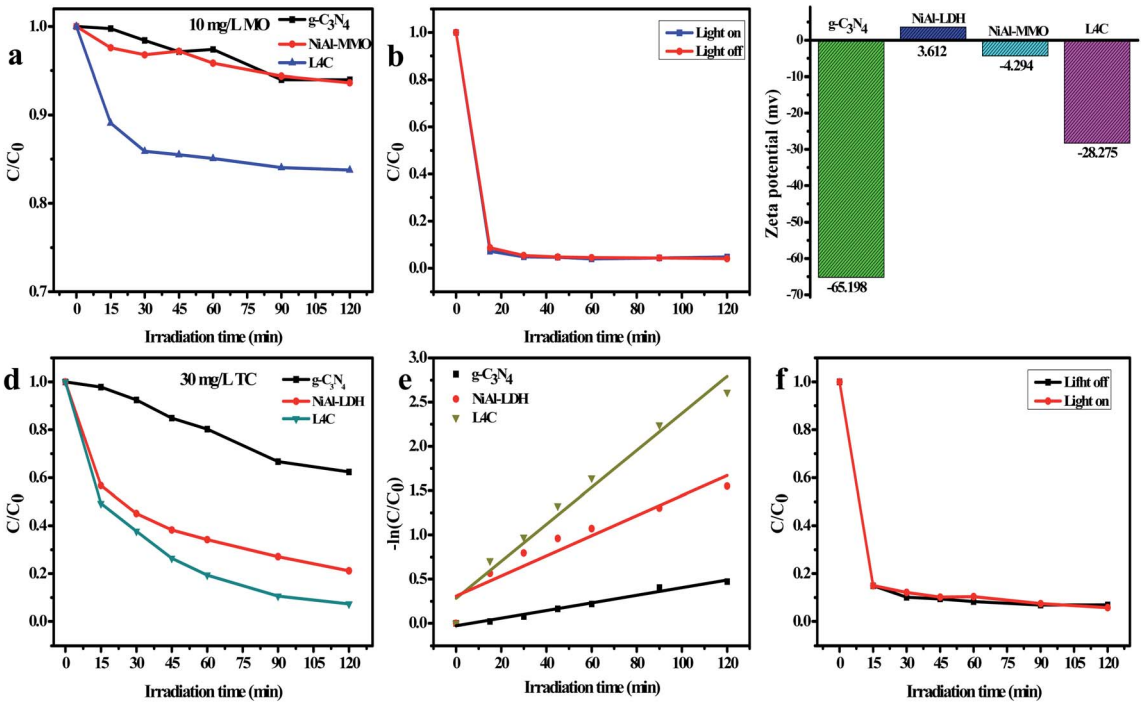

Fig. 11 Photocatalytic degradation of (a) 10 mg L^{-1} MO and (d) 30 mg L^{-1} TC. Adsorption and photodegradation experiment of (b) MO over NiAl-LDH and (f) TC over L4C samples. (c) Zeta potential. (e) The pseudo-first-order kinetic fitting curve of TC over the L4C sample.

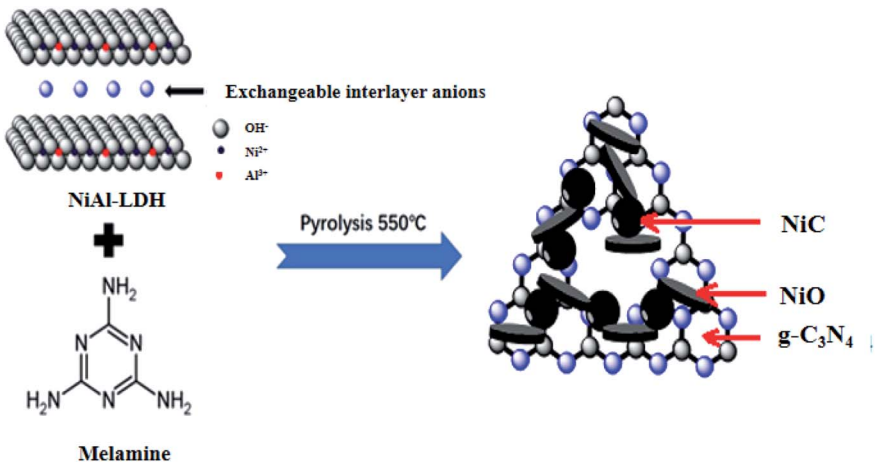

Fig. 12 Diagram of the formation of NiO/NiC/g-C_3N_4 nanocomposites.

composites produced by calcining the optimum mixture of NiAl-LDH and melamine. NiO is an inorganic metal-semiconductor with the characteristics of high chemical stability, low price, and good photocatalytic activity. Ni-metal carbides have the synergic advantages of being cost-effective with superior electric conductivity due to their alloy properties,[70] acting as highly efficient cocatalysts to improve the catalytic activity of the photocatalysts and electrocatalysts.

The nanocomposites consisting of two semiconductors (g-C_3N_4 and NiO) and one conductor (metallic NiC) are in keeping with the Z-scheme photocatalytic system (Fig. 13a). From the UV-Vis spectra in Fig. 6a, the band gap values of g-C_3N_4 and NiO were determined to be 2.61 and 3.27 eV, respectively. According to the Butler and Ginley model, CB and VB energies of the semiconductors at the points of zero charge can be calculated by the following equations:[71]

$$E_{CB} = E_{VB} - E_g \quad (1)$$

$$E_{VB} = X - E^e + 0.5E_g \quad (2)$$

where X is the absolute electronegativity of the semiconductor, E^e is the energy of free electrons on the hydrogen scale (4.5 eV), and E_g is the bandgap energy of the semiconductor.

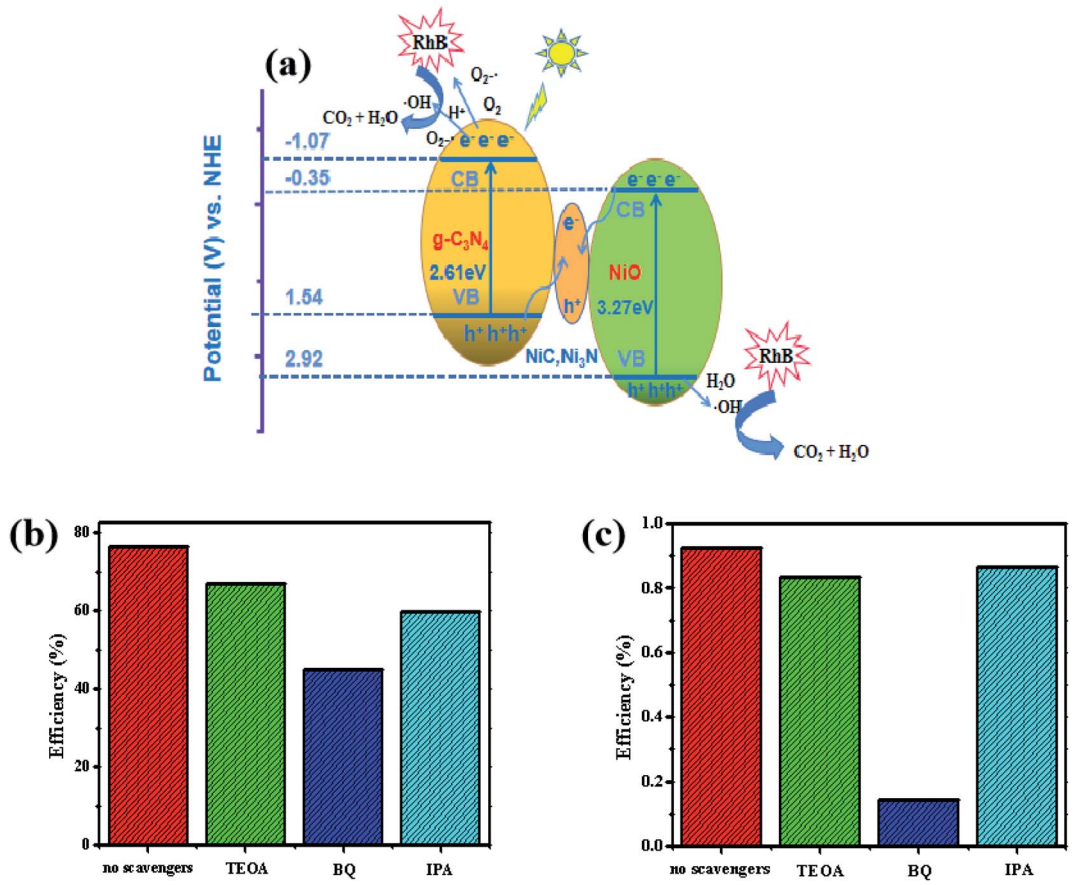

Fig. 13 (a) The mechanism of the photocatalytic degradation in NiO/NiC/g-C_3N_4, (b), (c) photocatalytic activities of L4C for the RhB and TC in the presence of scavengers.

The X value of NiO was reported earlier as 5.75 eV in the literature,[72,73] so the CB and VB energies were determined to be −1.07 and 1.54 eV for g-C_3N_4, and -0.35 eV and 2.92 eV for NiO, respectively. The more positive VB potential of NiO and more negative CB potential of g-C_3N_4 indicated[74,75] the photooxidation reaction *via* the VB holes of NiO and the photoreduction reaction *via* the CB electrons of g-C_3N_4 under irradiation. The metallic NiC acted as electron mediators and can rapidly transfer photogenerated electrons from the conduction band of NiO to the holes in the valence band of g-C_3N_4.[76]

The photogenerated electrons in the CB of g-C_3N_4 reacted with the dissolved O_2 molecules to generate $O_2^{\bullet-}$ because the potential of $O_2/O_2^{\bullet-}$ (−0.33 eV) is more positive than the potentials of the CB of the semiconductors. On the other hand, the potential of O_2/H_2O_2 (0.69 eV) is more positive than the CB potentials of g-C_3N_4 and NiO, indicating that the electrons in the CB can reduce O_2 to H_2O_2 and then form ˙OH radicals according to the following reactions: $O_2 + 2e^- + 2H^+ = H_2O_2$, $H_2O_2 + e^- = {}^{\bullet}OH + OH^-$. Furthermore, the VB holes (2.92 eV) from NiO can directly oxidize water and OH^- to form ˙OH radicals, because the VB oxidation potential is more positive than those of $OH^-/{}^{\bullet}OH$ (1.99 eV) and $H_2O/{\cdot}OH$ (2.37 eV).[77,78] The superoxide radical anion $O_2^{\bullet-}$, hydroxyl radical ˙OH, and the holes are known as the reactive species that facilitate the degradation of the organic pollutants into harmless products like CO_2 and H_2O.[64,79]

To further detect the main reactive oxidative species in the photocatalytic process, isopropanol (IPA), triethanolamine (TEOA), and benzoquinone (BQ) were used as the scavengers for hydroxyl radicals (˙OH), holes (h^+) and superoxide radicals ($O_2^{\bullet-}$), respectively. The scavenger dosages were determined as 10 mmol L^{-1} in the RhB solution of 50 mg L^{-1} and TC solution of 30 mg L^{-1}. As shown in Fig. 13b and c, the photodegradation efficiency decreased in the presence of the scavengers, implying that h^+, $O_2^{\bullet-}$ and ˙OH species were generated for the degradation. Particularly, the introduction of BQ greatly decreased the photodegradation efficiency in comparison with other scavengers, so $O_2^{\bullet-}$ is the most important reactive species in this experiment. To further verify the production of $O_2^{\bullet-}$, the ESR analysis of the DMPO–$O_2^{\bullet-}$ signal over the L4C sample was carried out and shown in Fig. S2.† There were no DMPO–$O_2^{\bullet-}$ characteristic peaks in the dark, while four strong DMPO–$O_2^{\bullet-}$ characteristic peaks appeared after 20 min of visible-light illumination, demonstrating that $O_2^{\bullet-}$ can be produced with the sample L4C under visible light irradiation, which can be used for the photocatalytic degradation of RhB and TC.

4. Conclusion

The novel NiO/NiC/g-C_3N_4 nanocomposites were successfully synthesized from NiAl-LDH and melamine by simple calcination; a Z-scheme system was constructed *via* incorporating the semiconductors (NiO and g-C_3N_4) with the conductors (NiC). The as-prepared composites showed tunable color and interior components, offering great advantages for photodegradation activity. The photocatalytic properties of the resulting nanocomposites depend on the loading of melamine and NiAl-LDH. The L4C sample in the ratio of 1 : 1 has many good characteristics including dark color, low interfacial charge transfer resistance, and low recombination of photogenerated carriers. This composite showed excellent degradation activity, reaching 97.5% toward RhB and 73.4% toward tetracycline under the irradiation of visible light. This work will open up new opportunities to develop novel Ni-containing compounds for high-performance catalysts.

Conflicts of interest

There are no conflicts to declare.

Acknowledgements

The authors gratefully acknowledge the financial support by the Open Research Program of Engineering Research Center of Nano-Geomaterials of Ministry of Education (Grant No. NGM2020KF017).

References

1 S. Shabbir, M. Faheem, N. Ali, P. G. Kerr and Y. Wu, *J. Bioresour. Technol.*, 2017, **225**, 395–401.
2 Z. Kim, C. Jeon, T. Hwa and C. Wonyong, *Appl. Catal., B*, 2018, **237**, 772–782.
3 E. Baylan and O. Altintas Yildirim, *Mater. Sci. Semicond. Process.*, 2019, **103**, 104621.
4 L. Liu, W. Wu, J. Zhang, P. Lv, L. Xu and C. Yan, *Acta Ecol. Sin.*, 2018, **38**, 36–41.
5 H. Wang, X. Yang, J. Zi, M. Zhou, Z. Ye, J. Li, Q. Guan, P. Lv, P. Huo and Y. Yan, *J. Ind. Eng. Chem.*, 2016, **35**, 83–92.
6 N. Y. Donkadokula, A. K. Kola, I. Naz and D. Saroj, *Rev. Environ. Sci. Bio/Technol.*, 2020, **19**, 543–560.
7 A. Thirunavukkarasu, R. Nithya and R. Sivashankar, *Rev. Environ. Sci. Bio/Technol.*, 2020, **19**, 751–778.
8 S. He, Z. An, M. Wei, D. G. Evans and X. Duan, *Chem. Commun.*, 2013, **49**, 5912–5920.
9 K. Abderrazek, F. S. Najoua and E. Srasra, *Appl. Clay Sci.*, 2016, **119**, 229–235.
10 A. Garcia-Gallastegui, D. Iruretagoyena, V. Gouvea, M. Mokhtar, A. M. Asiri, S. N. Basahel, S. A. Al-Thabaiti, A. O. Alyoubi, D. Chadwick and M. S. P. Shaffer, *Chem. Mater.*, 2012, **24**, 4531–4539.
11 J. L. White, M. F. Baruch, J. E. Pander III, Y. Hu, I. C. Fortmeyer, J. E. Park, T. Zhang, K. Liao, J. Gu, Y. Yan, T. W. Shaw, E. Abelev and A. B. Bocarsly, *Chem. Rev.*, 2015, **115**, 12888–12935.
12 M. Lan, G. Fan, L. Yang and F. Li, *RSC Adv.*, 2015, **5**, 5725–5734.
13 B. Ou, J. Wang, Y. Wu, S. Zhao and Z. Wang, *Chem. Eng. J.*, 2020, **380**, 122600.
14 M. Shao, J. Han, M. Wei, D. G. Evans and X. Duan, *Chem. Eng. J.*, 2011, **168**, 519–524.
15 X. Yuan and W. Li, *Appl. Clay Sci.*, 2017, **138**, 107–113.
16 E. Boorboor Azimi, A. Badiei and M. Hossaini Sadr, *J. Phys. Chem. Solids*, 2018, **122**, 174–183.
17 S. Ye, R. Wang, M. Z. Wu and Y. P. Yuan, *Appl. Surf. Sci.*, 2015, **358**, 15–27.
18 W. Liu, M. Wang, C. Xu and S. Chen, *Chem. Eng. J.*, 2012, **209**, 386–393.
19 H. Li, F. Li, J. G. Yu and S. W. Cao, *Acta Phys.-Chim. Sin.*, 2021, **37**, 2010073.
20 S. Tonda, S. Kumar, M. Bhardwaj, P. Yadav and S. Ogale, *ACS Appl. Mater. Interfaces*, 2018, **10**, 2667–2678.
21 J. Y. He, D. Zhang, X. J. Wang, J. Zhao, Y. P. Li, Y. Liu and F. T. Li, *Int. J. Hydrogen Energy*, 2021, **46**, 18977–18987.
22 Q. Shi, J. Huang, Y. Yang, J. Wu, J. Shen, X. Liu, A. Sun and Z. Liu, *Mater. Lett.*, 2020, **268**, 127560.
23 D. Sun, D. Chi, Z. Yang, Z. Xing, J. Yin, Z. Li, Q. Zhu and W. Zhou, *Int. J. Hydrogen Energy*, 2019, **44**, 16348–16385.
24 G. Di, Z. Zhu, Q. Huang, H. Zhang, J. Zhu, Y. Qiu, D. Yin and J. Zhao, *Sci. Total Environ.*, 2019, **650**, 1112–1121.
25 S. Patnaik, D. P. Sahoo, L. Mohapatra, S. Martha and K. Parida, *Energy Technol.*, 2017, **5**, 1687–1701.
26 X. Fan, Z. Peng, R. Ye, H. Zhou and X. Guo, *ACS Nano*, 2015, **9**, 7407–7418.
27 Z. Zhao, J. Wu, Y. Z. Zheng, N. Li and X. Tao, *ACS Catal.*, 2019, **9**, 8144–8152.
28 W. Zhang, W. Li, Y. Li, S. Peng and Z. Xu, *Catal. Today*, 2019, **335**, 326–332.
29 S. Deng, P. Yang, J. Xie, L. Ke, W. Liu and X. Chen, *Appl. Catal., B*, 2018, **2279**, 218–228.
30 K. He, J. Xie, Z. Yang, R. Shen, Y. Fang, S. Ma, X. Chen and X. Li, *Catal. Sci. Technol.*, 2017, **7**, 1193–1202.
31 B. Ma, H. Xu, K. Lin, L. Jin and C. Li, *ChemSusChem*, 2016, **47**, 820–824.
32 J. Ran, G. Gao, F. T. Li, T. Y. Ma, A. Du and S. Z. Qiao, *Nat. Commun.*, 2017, **8**, 13907.
33 H. Yang, S. Luo, X. Li, S. Li, J. Jin and J. Ma, *J. Mater. Chem. A*, 2016, **4**, 2–16.
34 J. Yin, Q. Fan, Y. Li, F. Cheng, P. Zhou, P. Xi and S. Sun, *J. Am. Chem. Soc.*, 2016, **138**, 14546–14549.
35 S. Geng, W. Yang and Y. Yu, *Chem.–Asian J.*, 2019, **14**, 1013–1020.
36 K. Xu, H. Ding, H. Lv, P. Chen, H. Cheng, T. Zhou, S. Liu, X. Wu and C. Wu, *Adv. Mater.*, 2016, **28**, 3326–3332.
37 H. Wang, Y. Cao, G. Zou, Q. Yi, J. Guo and L. Gao, *ACS Appl. Mater. Interfaces*, 2017, **9**, 60–64.
38 K. He, J. Xie, Z. Q. Liu, N. Li, X. Chen, J. Hu and X. Li, *J. Mater. Chem. A*, 2018, **6**, 13100.
39 L. Li, K. S. Hui, K. N. Hui, Q. Xia, J. Fu and Y. R. Cho, *J. Alloys Compd.*, 2017, **721**, 803–812.

40 X. Yuan, C. Zhou, Q. Jing, Q. Tang, Y. Mu and A. K. Du, *Nanomaterials*, 2016, **6**, 173.
41 S. Martha, A. Nashim and K. M. Parida, *J. Mater. Chem. A*, 2013, **1**, 7816.
42 S. C. Yan, Z. S. Li and Z. G. Zou, *Langmuir*, 2009, **25**, 10397–10401.
43 L. Zhang, K. N. Hui, K. S. Hui, X. Chen, R. Chen and H. Lee, *Int. J. Hydrogen Energy*, 2016, **41**, 9443–9453.
44 Z. Lv, S. Yang, H. Zhu, L. Chen, N. S. Alharbi, M. Wakeel, A. Wahid and C. Chen, *Appl. Surf. Sci.*, 2018, **448**, 599–608.
45 W. Zhang, W. Li, Y. Li, S. Peng and Z. Xu, *Catal. Today*, 2019, **335**, 326–332.
46 X. Shi, X. Wen, S. Nie, J. Dong, J. Li, Y. Shi, H. Zhang and G. Bai, *J. Catal.*, 2020, **382**, 22–30.
47 S. Prasad Adhikari, H. Raj Pant, H. Joo Kim, C. Hee Park and C. Sang Kim, *Ceram. Int.*, 2015, **41**, 12923–12929.
48 S. P. Adhikari, H. R. Pant, J. H. Kim, H. J. Kim, C. H. Park and C. S. Kim, *Colloids Surf., A*, 2015, **482**, 477–484.
49 K. He, J. Xie, Z. Q. Liu, N. Li, X. Chen, J. Hu and X. Li, *J. Mater. Chem. A*, 2018, **6**, 13110–13122.
50 R. M. M. Dos Santos, R. G. L. Gonçalves, V. R. L. Constantino, L. M. Da Costa, L. H. M. Da Silva, J. Tronto and F. G. Pinto, *Appl. Clay Sci.*, 2013, **80**, 189–195.
51 J. Ma, J. Ding, L. Yu, L. Li, Y. Kong and S. Komarneni, *Appl. Clay Sci.*, 2015, **7**, 85–89.
52 S. Tian, Q. Fu, W. Chen, Q. Feng, Z. Chen, J. Zhang, W. C. Cheong, R. Yu, L. Gu, J. Dong, J. Luo, C. Chen, Q. Peng, C. Draxl, D. Wang and Y. Li, *Nat. Commun.*, 2018, **9**, 2353.
53 Y. Wang, L. Chen, X. Yu, Y. Wang and G. Zheng, *Adv. Energy Mater.*, 2017, **7**, 672–677.
54 M. Irfan, I. U. Khan, J. Wang, Y. Li and X. Liu, *RSC Adv.*, 2020, **10**, 6444–6451.
55 X. Yu, J. Zhang, Z. Zhao, W. Guo, J. Qiu, X. Mou, A. Li, J. P. Claverie and H. Liu, *Nano Energy*, 2015, **16**, 207–217.
56 Z. Sun, H. Chen, L. Zhang, D. Lu and P. Du, *J. Mater. Chem. A*, 2016, **4**, 13289–13295.
57 S. Tonda, S. Kumar, Y. Gawli, M. Bhardwaj and S. Ogale, *Int. J. Hydrogen Energy*, 2017, **42**, 5971–5984.
58 Y. Yang, Z. Peng, A. Muhammad, H. Wang, W. Wang, Z. Wu, Z. Wang, X. Qiu, H. Tan and H. Liu, *ACS Sustainable Chem. Eng.*, 2018, **6**, 11587–11594.
59 S. Ma, Y. Deng, J. Xie, K. He, W. Liu, X. Chen and X. Li, *Appl. Catal., B*, 2018, **227**, 218–228.
60 C. An, M. Nakaya, K. Kanie and A. Muramatsu, *Nanosci. Nanotechnol. Lett.*, 2017, **9**, 1592–1595.
61 S. P. Adhikari, G. P. Awasthi, J. Lee, C. H. Park and C. S. Kim, *RSC Adv.*, 2016, **6**, 55079–55091.
62 F. Zhang, C. L. Zhang, L. Song, R. C. Zeng, L. Y. Cui and H. Z. Cui, *Acta Metall. Sin.*, 2015, **28**, 1373–1381.
63 N. Benjamin A, *ACS Nano*, 2015, **5**, 5135–5142.
64 M. A. Karimi, M. Atashkadi, M. Ranjbar and A. Habibi-Yangjeh, *Arab. J. Chem.*, 2020, **13**, 5810.
65 P. Chaudhary and P. P. Ingole, *Int. J. Hydrogen Energy*, 2020, **45**, 16060–16070.
66 J. Yin, Q. Fan, Y. Li, F. Cheng, P. Zhou, P. Xi and S. Sun, *J. Am. Chem. Soc.*, 2016, **138**, 14546–14549.
67 W. Yu, X. Liu, L. Pan, J. Li, J. Liu, J. Zhang, P. Li, C. Chen and Z. Sun, *Appl. Surf. Sci.*, 2014, **319**, 107–112.
68 Y. Miao, R. Guo, J. Gu, Y. Liu, G. Wu, C. Duan, X. Zhang and W. Pan, *Appl. Surf. Sci.*, 2020, **527**, 146792.
69 Y. Guo, X. Liu, X. Dong, A. Lqbal, C. Yang, W. Liu and W. Qin, *RSC Adv.*, 2015, **116**, 95495–95503.
70 K. Xu, H. Ding, H. Lv, P. Chen, X. Lu, H. Cheng, T. Zhou, S. Liu, X. Wu, C. Wu and Y. Xie, *Adv. Mater.*, 2016, **28**, 3326–3332.
71 W. J. Ong, L. L. Tan, Y. H. Ng, S. T. Yong and S. P. Chai, *Chem. Rev.*, 2016, **116**, 7159–7329.
72 Z. Yousaf, S. Sajjad, S. Ahmed Khan Leghari, M. Mehboob, A. Kanwal and B. Uzair, *J. Solid State Chem.*, 2020, **291**, 121606.
73 R. M. Mohamed and F. A. Harraz, *Mater. Res. Bull.*, 2020, **131**, 110965.
74 Y. Li, H. Zhang, P. Liu, D. Wang, Y. Li and H. Zhao, *Small*, 2013, **9**, 3336–3344.
75 L. Sun, M. Yang, J. Huang, D. Yu, W. Hong and X. Chen, *Adv. Funct. Mater.*, 2016, **26**, 4943–4950.
76 J. Liu, W. Fang, Z. Wei, Z. Qin, Z. Jiang and W. Shangguan, *Appl. Catal., B*, 2018, **238**, 465–470.
77 S. Wang, D. Li, C. Sun, S. Yang, Y. Guan and H. He, *Appl. Catal., B*, 2014, **144**, 885–892.
78 S. Huang, J. Zhong, J. Li, J. Chen, Z. Xiang, W. Hu and M. Li, *Mater. Res. Bull.*, 2016, **84**, 65–70.
79 T. Liu, M. Li, P. Dong, Y. Zhang and M. Zhou, *Sens. Actuators, B*, 2018, **260**, 962–975.